ADVANCED MATERIALS
www.advmat.de

Check for updates

Stochastically Broken Inversion Symmetry of Van der Waals Topological Insulator for Nanoscale Physically Unclonable Functions

Gunhyoung Kim, Jinhyoung Lee, Hyunho Seok, Taewoo Kang, Minyoung Lee, Hyunbin Choi, Sihoon Son, Jinill Cho, Dongho Lee, Seowoo Son, Hosin Hwang, Hyelim Shin, Sujeong Han, Gunhoo Woo, Alexina Ollier, Yeon-Ji Kim, Lei Fang, Seunghwan Lee, Gyuho Han, Goo-Eun Jung, Youngi Lee, Hyeong-U. Kim, Jungwon Park, Andreas Heinrich, Won-Jun Jang, Seok Joon Kwon, and Taesung Kim**

Owing to the exotic state of quantum matter, topological insulators have emerged as a significant platform for new-generation functional devices. Among these topological insulators, tetradymites have received significant attention because of their van der Waals (vdW) structures and inversion symmetries. Although this inversion symmetry completely blocks exotic quantum phenomena, it should be broken down to facilitate versatile topological functionalities. Recently, a Janus structure is suggested for asymmetric out-of-plane lattice structures, terminating the heterogeneous atoms at two sides of the vdW structure. However, the synthesis of Janus structures has not been achieved commercially because of the imprecise control of the layer-by-layer growth, high-temperature synthesis, and low yield. To overcome these limitations, plasma sulfurization of vdW topological insulators has been presented, enabling stochastic inversion asymmetry. To take practical advantage of the random lattice distortion, physically unclonable functions (PUFs) have been suggested as applications of vdW Janus topological insulators. The sulfur dominance is experimentally demonstrated via X-ray photoelectron spectroscopy, hysteresis variation, cross-sectional transmission electron microscopy, and adhesion energy variation. In conclusion, it is envisioned that the vdW Janus topological insulators can provide an extendable encryption platform for randomized lattice distortion, offering on-demand stochastic inversion asymmetry via a single-step plasma sulfurization.

1. Introduction

Since the discovery of topological insulators, topological protection has emerged as a systematic platform for versatile advances in spintronics and condensed matter physics.[1] Topological insulation offers a new type of quantum phenomena with an insulating bulk state and gapless Dirac-type edge states.[2] Owing to their bulk band structure, 3D topological insulators possess a massless Dirac dispersion with spin–momentum locking at the surface, which enables a gapless state and low effective mass in bulk insulation.[3] Regarding the topological protection rule, the topological states are protected by spin-orbit coupling (SOC)[4] and time-reversal symmetry (TRS).[4,5] Among these topological insulators, tetradymites M_2X_3 (M = Bi, Sb; X = Se, Te) have been constructed with heavy p-block elements and their corresponding strong SOC, which can concurrently provide a van der Waals (vdW) structure with topological protection.[6] Using vdW topological insulators, 3D integration for functional quantum device applications, including field-effect transistors,[7]

G. Kim, H. Choi, H. Hwang, H. Shin, S. Han, T. Kim
Department of Semiconductor Convergence Engineering
Sungkyunkwan University
Suwon 16419, South Korea
E-mail: tkim@skku.edu

J. Lee, J. Cho, D. Lee, S. Lee, T. Kim
School of Mechanical Engineering
Sungkyunkwan University (SKKU)
Suwon-si, Gyeonggi-do 16419, South Korea

The ORCID identification number(s) for the author(s) of this article can be found under https://doi.org/10.1002/adma.202419927

DOI: 10.1002/adma.202419927

J. Lee, A. Ollier, Y.-J. Kim, L. Fang, A. Heinrich, W.-J. Jang
Center for Quantum Nanoscience
Institute for Basic Science (IBS)
Seoul 03760, South Korea

H. Seok, S. Son, S. Son, G. Woo, T. Kim
SKKU Advanced Institute of Nanotechnology (SAINT)
Sungkyunkwan University
Suwon 16419, South Korea

H. Seok, S. Son, S. Son, G. Woo, T. Kim
Department of Nano Science and Technology
Sungkyunkwan University
Suwon 16419, South Korea

© 2025 Wiley-VCH GmbH

photodetectors,[8] memristors,[9] thermal devices,[10] and plasmonic nanostructures,[11] has been achieved.

Nevertheless, vdW topological insulators exhibit a symmetrical structure that completely blocks their potential for unique electronic dynamics and applications in spin-orbit devices.[12] To preserve topological protection, the inversion symmetry must be broken for versatile functionalities in topological applications.[13] When the inversion symmetry is broken, a variety of quantum functionalities can be activated, including second-harmonic generation,[14] Hall effects,[7b,15] ferroelectricity,[16] flexoelectricity,[17] and bulk photovoltaic effects.[18] Furthermore, symmetry breaking in vdW materials can integrate heterogeneously broken symmetries into the same system, paving the way to unveil unconventional quantum phenomena.[19] To break the inversion symmetry extensively, vdW heterostructures have been widely used to manipulate exotic quantum properties.[20] However, vdW heterostructures have critical limitations at the interfacial contact, including defects,[16a] electrical leakage,[21] charge traps,[22] and interlayer atomic diffusion.[23] Moreover, conventional vdW heterostructures can be fabricated via mechanical exfoliation and 3D stacking processes, which are unsuitable for large-scale production and commercialization.[23]

To overcome the limitations of vdW heterostructures, a Janus structure has been suggested for asymmetric out-of-plane (OOP) lattice structures, terminating the heterogeneous atoms on two sides of the vdW structure, such as $M_2(SSe)_3$ (M = Bi, Sb).[24] Regarding the synthesis of Janus structures, the conventional limitations of vdW heterojunctions can be overcome, allowing the stochastic inversion asymmetry without structural degradation with direct synthesis.[25] Nonetheless, the direct synthesis of Janus structures has not been widely commercialized owing to three major limitations: i) precise kinetic control of layer-by-layer growth,[26] ii) high-temperature synthesis,[27] and iii) large-scale controllability of the layer and crystallinity.[28] The intrinsic limitations of the Janus structure motivated us to develop an on-demand synthesis method and its corresponding applications.[29]

Herein, we present a vdW Janus topological insulator for stochastic inversion asymmetry via plasma sulfurization, which enables large-scale sulfurization.[30] During plasma sulfurization, the Se atom of the top layer is terminated by an S atom, which enables the synthesis of a randomized Janus structure.[29a,31] By constructing an atomic force microscopy (AFM) junction with sulfurized Bi_2Se_3, the piezoelectric force microscopy (PFM) hysteresis,[32] OOP domain,[33] work function,[34] and adhesion energy were spatially probed,[35] exhibiting sulfur dominance with an increase in radio frequency (RF) plasma power.[36] To take practical advantage of the stochastic inversion asymmetry, sulfurized Bi_2Se_3 has been regarded as a physically unclonable function (PUFs) that can be utilized for encryption applications with challenge-response pairs (CRPs) generation.[37] While the practical application of topological insulators is completely hindered by the topological protection rule, plasma sulfurization activates OOP domain randomness, which permits the practical application of topological insulators that was not previously possible. In conclusion, we envision that our Janus PUFs platform can offer an extendable and systematic platform for stochastic inversion asymmetry in large-scale production and contact-free symmetry breaking.

2. Results and Discussion

2.1. vdW Janus Topological Insulator Platform for Stochastically Broken Symmetry

To break the inversion symmetry on the surface of the topological insulators Bi_2Se_3, single-step penetrative plasma sulfurization has been utilized to synthesize the stochastic Janus topological insulator via hydrogen sulfide (H_2S) + argon (Ar) ion bombardment, which breaks the inversion symmetry of the top layer of Bi_2Se_3 (Figures S1 and S2, Supporting Information). As shown in **Figure 1a**, the Janus PUFs were fabricated in the following three steps. First, Bi_2Se_3 was mechanically exfoliated and transferred onto a SiO_2/Si wafer. While the pristine Bi_2Se_3 exhibited topological protection, which consists of bulk insulating state and edge conduction, the bulk Bi_2Se_3 was selected for Janus PUFs fabrication. Second, single-step penetrative plasma sulfurization was conducted to randomly generate inversion symmetry breaking in bulk Bi_2Se_3. Third, the PFM junction was constructed for nanoscale observation of the stochastic OOP domain distribution with direct current (DC) sample bias, alternating current (AC) tip bias, 2 lock-in amplifiers for OOP and in-plane, and AFM system. Furthermore, cross-sectional transmission electron microscopy (TEM) images and their corresponding selected area diffraction (SAED) patterns were experimentally obtained to validate the

T. Kang, S. J. Kwon
School of Chemical Engineering
Sungkyunkwan University
Sungkyunkwan University
Suwon 16419, South Korea
E-mail: sjoonkwon@skku.edu
M. Lee, J. Park
School of Chemical and Biological Engineering
Institute of Chemical Process
Seoul National University
Seoul 08826, South Korea
A. Ollier, Y.-J. Kim, A. Heinrich, W.-J. Jang
Department of Physics
Ewha Womans University
Seoul 03760, South Korea
G. Han, G.-E. Jung, Y. Lee
Park Systems Corporation
109, Gwanggyo-ro, Yeongtong-gu, Suwon-si, Gyeonggi-do 16229, South Korea
H.-U. Kim
Semiconductor Manufacturing Research Center
Korea Institute of Machinery and Materials (KIMM)
Daejeon 34103, South Korea
H.-U. Kim
Nano-Mechatronics
KIMM Campus
University of Science & Technology (UST)
Daejeon 34113, South Korea
J. Park
Center for Nanoparticle Research
Institute for Basic Science (IBS)
Seoul 08826, South Korea
T. Kim
Department of Nano Engineering
Sungkyunkwan University
Suwon 16419, South Korea

© 2025 Wiley-VCH GmbH

15214095, 0, Downloaded from https://advanced.onlinelibrary.wiley.com/doi/10.1002/adma.202419927 by Seoul National University, Wiley Online Library on [25/02/2025]. See the Terms and Conditions (https://onlinelibrary.wiley.com/terms-and-conditions) on Wiley Online Library for rules of use; OA articles are governed by the applicable Creative Commons License

15214095, 0, Downloaded from https://advanced.onlinelibrary.wiley.com/doi/10.1002/adma.202419927 by Seoul National University, Wiley Online Library on [25/02/2025]. See the Terms and Conditions (https://onlinelibrary.wiley.com/terms-and-conditions) on Wiley Online Library for rules of use; OA articles are governed by the applicable Creative Commons License

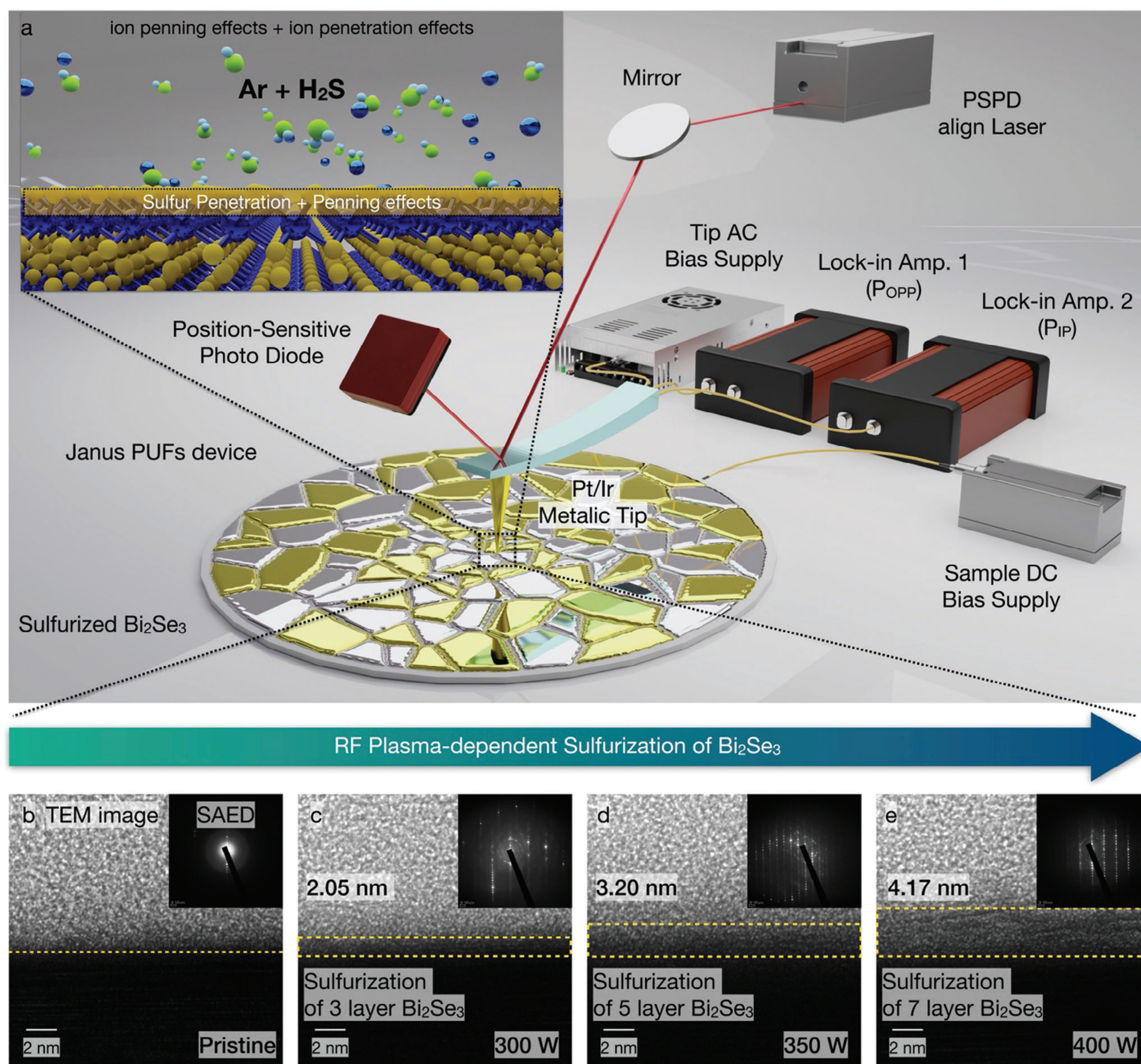

Figure 1. vdW Janus topological insulator Bi_2Se_3 with stochastically broken symmetry via plasma sulfurization. a) Schematic illustration of the vdW Janus PUF platform, which has been achieved with i) Ar + H_2S plasma sulfurization and ii) OOP PFM junction. To spatially resolve the polarization distribution, the PFM junction has been vertically constructed with AC tip bias, DC sample bias, and Pt/Ir tip. Cross-sectional TEM image of sulfurized Bi_2Se_3 with b) RF plasma 0 W, c) RF plasma 300 W (Sulfurized vdW 3-layer thickness as 2.05 nm), d) RF plasma 350 W (Sulfurized vdW 5-layer thickness as 3.20 nm), and e) RF plasma 400 W (Sulfurized vdW 7-layer thickness as 4.17 nm), indicating the sequential expansion of Bi_2Se_3 with penetrative sulfurization.

sulfurization of the Bi_2Se_3 top layer and its corresponding lattice distortion (Figure S3, Supporting Information), as shown in Figure 1b–e. Sulfurized Bi_2Se_3 layer thickness varies as 2.05 nm (vdW 3-layer thickness, 300 W), 3.20 nm (vdW 5-layer thickness, 350 W), and 4.17 nm (vdW 7-layer thickness, 400 W), indicating the sequential sulfurization of cross-sectional vdW layer configuration. As the RF plasma power increased, the stochastic lattice distortion was correlated with the sequential expansion and cross-sectional energy-dispersive X-ray spectroscopy (EDS) mapping of the Bi_2Se_3 quintuple layer (QL)\, which is attributed to the penetrative sulfurization (Figure S4, Supporting Information). To further clarify the uniformity of the sulfurized region of Bi_2Se_3, large-scale uniformity was clearly observed via a cross-sectional TEM image of sulfurized Bi_2Se_3 with RF 400 W plasma (Figure S5, Supporting Information). As the sulfurization depth depends on RF power variation, the sulfurization percentage of each vdW layer may exhibit the heterogenous sulfurization percentage. Thus, cross-sectional TEM intensity mapping with RF 400 W sulfurized Bi_2Se_3 results in 7-layer sulfurization. A linear decrease in sulfurization percentage was observed, resulting

© 2025 Wiley-VCH GmbH

in a 63.18% decrease in the 7th layer, compared with a top layer of sulfurized Bi_2Se_3 with RF 400 W plasma (Figure S6, Supporting Information). Owing to the previous,[29a] the ion penning effect has been activated with ion bombardment and ion penetration, which is specialized to control the lattice structure and interface characteristics. While the relatively larger amount of ion can be penetrated through the Bi_2Se_3 surface, compared with the pre-deposited Mo/W metal layer, sulfurization of Bi_2Se_3 can be successfully achieved without damage to the Bi atom of the top layer.

2.2. Sequential Observation of Sulfurization in vdW Janus Topological Insulator

X-ray photoelectron spectroscopy (XPS) measurements were performed to clarify the variation of chemical bonding via plasma sulfurization, as shown in **Figure** 2a. The Bi *4f* XPS spectra of pristine Bi_2Se_3 indicated a binding energy of 161.2 and 166.5 eV, and the XPS spectra with RF power variation exhibited the Bi—S bonding formation. When RF plasma was applied to pristine Bi_2Se_3, Bi—S bonding and its corresponding Bi—S and Se—S bonding peaks were sequentially generated and increased at 160.1 and 166.2 eV. The sulfur dominance in the top layer of the Bi_2Se_3 QL is illustrated in Figure 2b. Owing to the ion bombardment, Se atoms were terminated by S atoms via randomized S atom penetration, which resulted in a substantial increase in sulfur dominance and randomized lattice distortion. As the binding energy of S *2p* and Bi *4f* overlap, we have comprehensively displayed S *2p* and Bi *4f* spectra in Figure 2a. Furthermore, XPS spectra of S *2p* have been separately displayed (Figure S7, Supporting Information). Moreover, the surface state of sulfurized Bi_2Se_3 can be correlated with Kelvin probe force microscopy (KPFM) imaging,[17] which provides the correlative surface roughness, work function, and electrical potential mapping of sulfurized Bi_2Se_3. The pixel distribution of the surface roughness (Figure 2c) exhibits corresponding results with the 3D topography image and RF plasma power variation (Figure 2f–i). Furthermore, the work function (Figure 2d) and electrical potential mapping (Figure 2e) provided indirect evidence of sulfur dominance. While the electrical potential of pristine Bi_2Se_3 (313.0 mV) decreased to 201.02 mV (300 W), 105.78 mV (350 W), and −126.53 mV (400 W), the work function of pristine Bi_2Se_3 has increased from 4.88 eV (pristine) to 4.99 eV (300 W), 5.08 eV (350 W), and 5.32 eV (400 W) within RF power variation. The electronegativity of the S atom was reported to be 2.58, whereas that of the Se atom was ≈2.55. Hence, the sulfurized Bi_2Se_3 resulted in a decreased work function owing to the higher electronegativity of the S atom, which indirectly indicates the dominance of sulfur in the top layer of the Bi_2Se_3 QL. In our sulfurization system, the sufficient generation of H_2S^+ for bombardment on Bi_2Se_3 to break the lattice is most crticial factor. The proposed mechanism of H_2S^+ generation in this system is the Penning effect by the Ar gas and the direct ionization of H_2S as follows Equations (1) and (2).[38]

$$Ar + e^- \rightarrow Ar^+ + 2e^- \quad (1)$$

$$Ar^+ + H_2S \rightarrow Ar + H_2S^+ \quad (2)$$

Sufficient electrons in the plasma system can directly ionize H_2S gas to generate H_2S^+, as shown in Equation (3). But except for Ar gas, it is difficult to generate H_2S plasma owing to the low ionization energy characteristics of H_2S gas.[39]

$$e^- + H_2S^+ \rightarrow 2e^- \quad (3)$$

For the precise control of plasma-based sulfurization, a moderate gas mixture ratio was set for Ar and H_2S as 1:1 (we injected 50 sccm for each gas). This ratio might influence the sulfurization process owing to the Penning ionization mechanism as mentioned above, but in current research, we focused on the plasma power effect on lattice breaking in Bi_2Se_3. Under a fixed gas mixture, plasma power has been controlled, which modulates the electrical field (E-field) in the sheath region. As increased the plasma power, the increased E-field results accelerated H_2S^+ onto Bi_2Se_3 with the higher ion bombardment resulting in further deep penetration of H_2S^+ for the sulfurization.

2.3. Adhesion Energy Mapping for Comparison of Pt—S/Pt—Se Bonding Strengths

To experimentally observe the sulfur dominance of sulfurized Bi_2Se_3, force-distance (FD) curve spectroscopy was spatially measured via platinum tip. The FD curve spectroscopy consists of three steps, which are classified as i) approach, ii) contact, and iii) retract, as illustrated in **Figure** 3a. In the i) approach section, the Pt tip slightly approached the sulfurized Bi_2Se_3 with nanoscale precision. Subsequently, the Pt tip interacted with the sample surface. In the ii) contact state, the deflection of the cantilever was temporarily recorded as an FD curve. In the iii) retraction section, the Pt tip retracts from the sulfurized Bi_2Se_3 via mechanical detachment, which directly describes the chemisorption/physisorption strengths of the Pt tip and sulfurized Bi_2Se_3. Upon retraction of the Pt tip, the interactions can be measured to describe the adhesion energy, Young's modulus, and energy dissipation of the sulfurized Bi_2Se_3. The time-dependent Z-position of the AFM tip is shown in Figure 3b. The force was maintained at 0 nN until 0.81 s, but it decreased to ≈−10 nN when the tip and sample were contacted. Subsequently, the force was increased to 90 nN with slight nanoindentation. Additionally, the tip moved upward after 1.00 s, and the force decreased to its lowest value, exhibiting detachment of the tip and the sample. Subsequently, it returned to 0 nN after 1.24 s. While the AFM tip was used to probe a pixel grid of FD curves at the sulfurized Bi_2Se_3, the Pt tip systematically measured the localized interactions with nanoscale precision and sensitivity,[40] as shown in Figure 3c–f. As the pristine Bi_2Se_3 exhibits constant adhesion energy (3.02×10^{-16} J) in the pristine Bi_2Se_3 layer (Figure 3c), spatial adhesion mapping experimentally shows the effect of sulfurization of Bi_2Se_3, as shown in Figure As the adhesion characteristic is attributed to the chemical composition of the Bi_2Se_3 QL, only Pt—Se bonding was generated during the AFM tip contact in the case of pristine Bi_2Se_3. During 300 W sulfurization, the S atom partially terminated the Se atom, maintaining Se dominance. In this situation, Pt—S bonding has been activated owing to the S atom existence, which exhibits higher adhesion

© 2025 Wiley-VCH GmbH

15214095, 0, Downloaded from https://advanced.onlinelibrary.wiley.com/doi/10.1002/adma.202419927 by Seoul National University, Wiley Online Library on [25/02/2025]. See the Terms and Conditions (https://onlinelibrary.wiley.com/terms-and-conditions) on Wiley Online Library for rules of use; OA articles are governed by the applicable Creative Commons License

15214095, 0, Downloaded from https://advanced.onlinelibrary.wiley.com/doi/10.1002/adma.202419927 by Seoul National University, Wiley Online Library on [25/02/2025]. See the Terms and Conditions (https://onlinelibrary.wiley.com/terms-and-conditions) on Wiley Online Library for rules of use; OA articles are governed by the applicable Creative Commons License

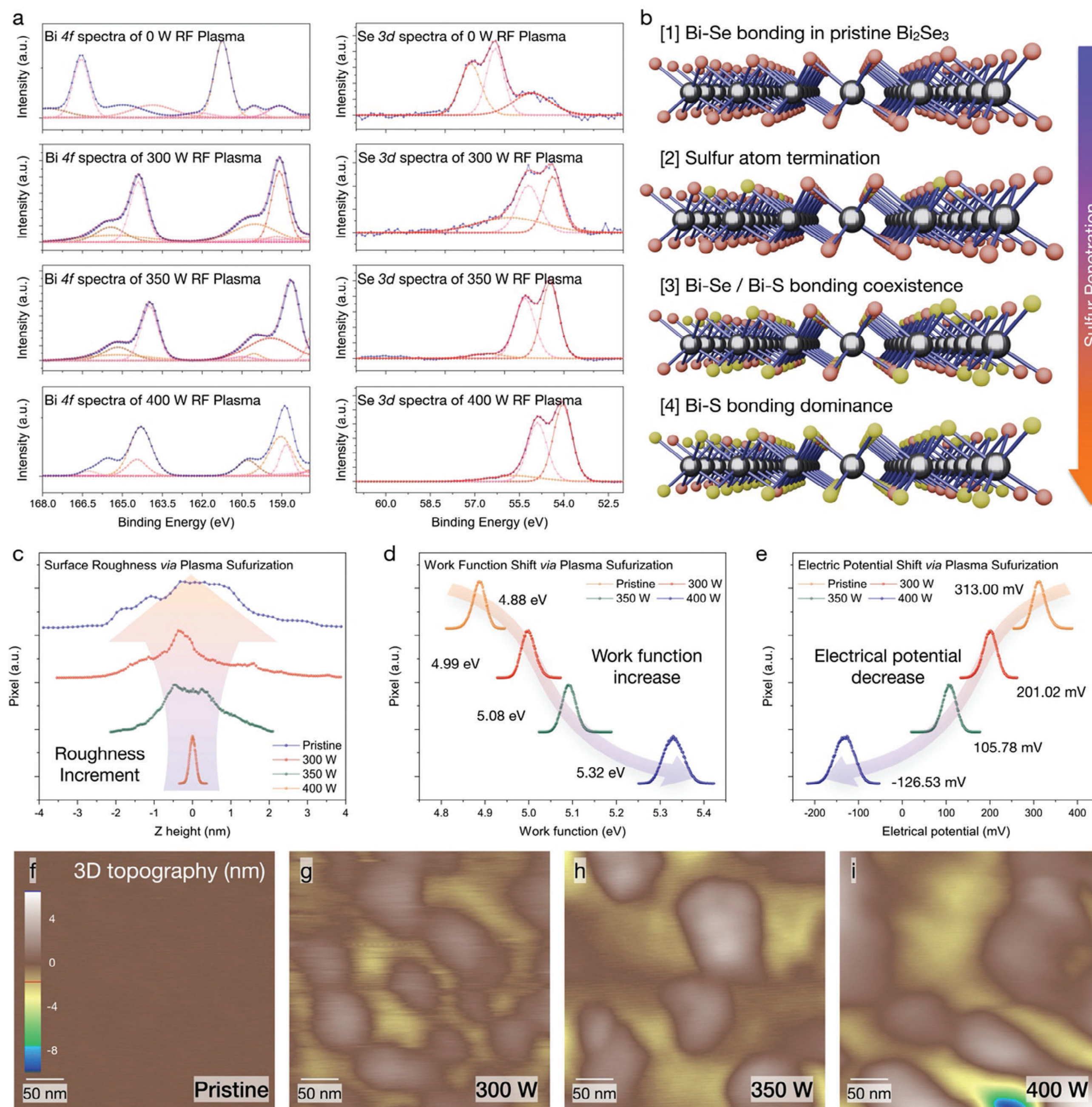

Figure 2. Sequentially-resolved sulfur dominance of RF plasma power variation in sulfurized Bi_2Se_3. XPS spectra cascade of a) Bi *4f* peak and S *2p* peak with RF plasma power variation, which is attributed to sulfur dominance of Bi_2Se_3 surface. b) Schematic illustration of sequential sulfurization process of Bi_2Se_3. Pixel distribution of c) surface roughness, d) work function, and e) electrical potential distribution of sulfurized Bi_2Se_3, which has been measured via Kelvin probe force microscopy. AFM topography image of sulfurized Bi_2Se_3 with f) RF plasma 0 W, g) RF plasma 300 W (Roughness as 0.598 nm), h) RF plasma 350 W (Roughness as 0.911 nm), and i) RF plasma 400 W (Roughness as 1.158 nm), resulting the increment of the defective topographical domain size.

energy (3.18×10^{-16} J) than pristine Bi_2Se_3 and higher electronegativity compared with the Se atom. When the RF plasma power was increased to 350 W, Pt—S bonding and Pt—Se bonding coexisted, resulting in an increase in the adhesion energy to 4.18 $\times 10^{-16}$ J. In RF plasma 400 W condition, Pt—S bonding becomes dominant compared with Pt—Se bonding, which leads to the maximized adhesion energy as 7.59×10^{-16} J. Furthermore, spatial adhesion mapping exhibits the randomness of the adhesion energy and adhesion force between the tip and sulfurized Bi_2Se_3, as shown in Figure 3g–i (Figure S8, Supporting Information). The adhesion energy can be extracted from the surrounding area between the tip approach curve and the tip retract curve. As the bonding strength of Pt—S bonding is relatively larger than Pt—Se bonding owing to the lower electronegativity

© 2025 Wiley-VCH GmbH

15214095, 0, Downloaded from https://advanced.onlinelibrary.wiley.com/doi/10.1002/adma.202419927 by Seoul National University, Wiley Online Library on [25/02/2025]. See the Terms and Conditions (https://onlinelibrary.wiley.com/terms-and-conditions) on Wiley Online Library for rules of use; OA articles are governed by the applicable Creative Commons License

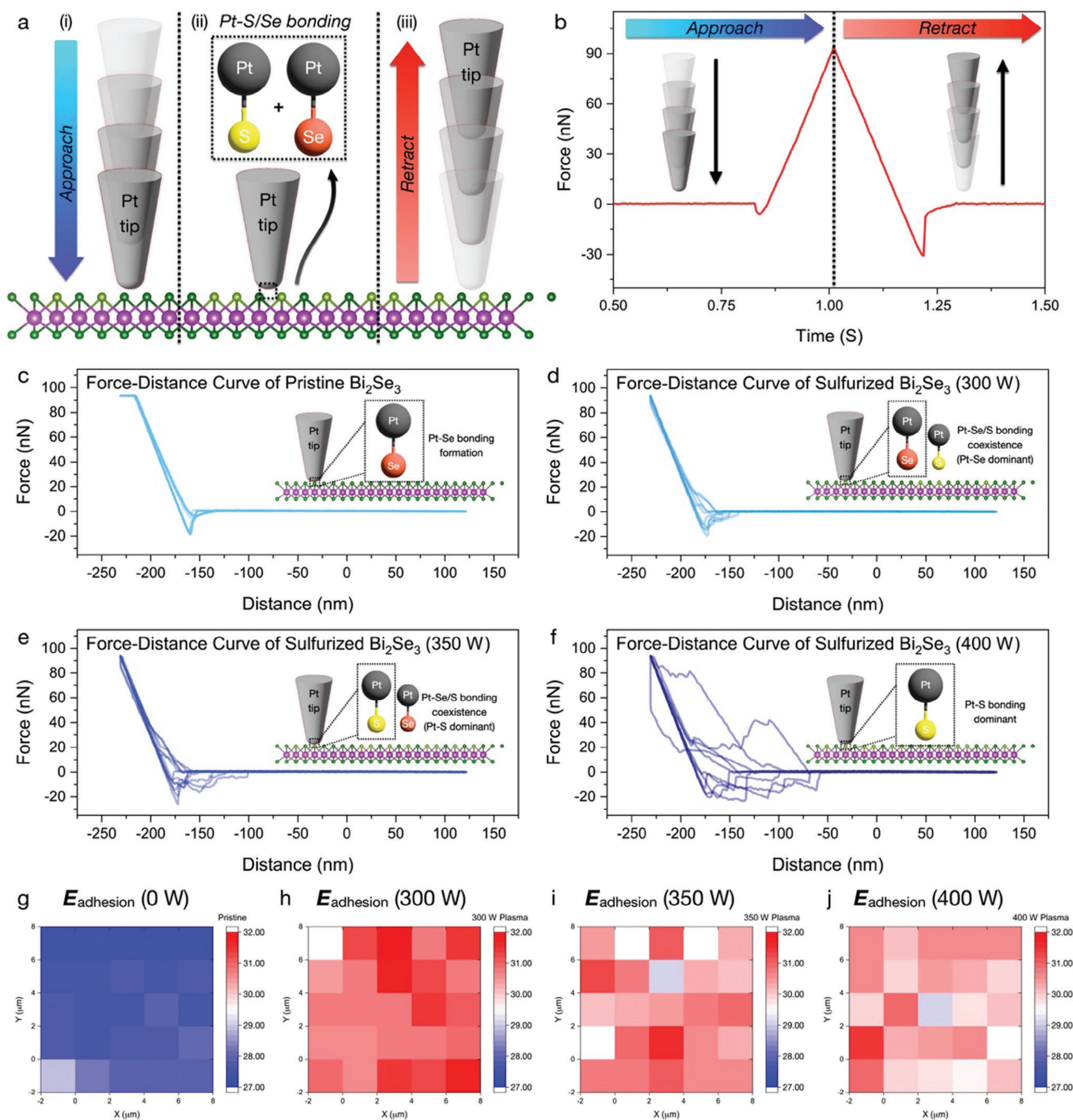

Figure 3. Spatially-resolved sulfur dominance via local adhesion energy distribution. a) Schematic illustration of the force-distance curve measurement and its corresponding b) time-dependent Z position of AFM cantilever. Force-distance curve mapping of sulfurized Bi_2Se_3 with c) RF plasma 0 W, d) RF plasma 300 W, e) RF plasma 350 W, and f) RF plasma 400 W (5 repetitive measurements). Spatially-resolved adhesion energy variation of 5 × 5 pixel grid with RF plasma variation as g) RF plasma 0 W, h) RF plasma 300 W, i) RF plasma 350 W, and j) RF plasma 400 W.

value of the Se atom, variation of adhesion energy also corresponds to the RF plasma power. Thus, the upper shift of the tip retract curve directly indicates the activation of chemical interaction between the Pt tip and sulfurized Bi_2Se_3, which demonstrates the spatial randomness via S atom termination at the Bi_2Se_3 top layer.

2.4. Controllable OOP Domain Size in Janus Bi_2Se_3 via RF Plasma Power Variation

As shown in **Figure** 4a–d, spatial OOP domain distribution was observed with the RF plasma variation, including PFM phase image (Figure 4a), PFM amplitude image (Figure 4b), PFM phase

© 2025 Wiley-VCH GmbH

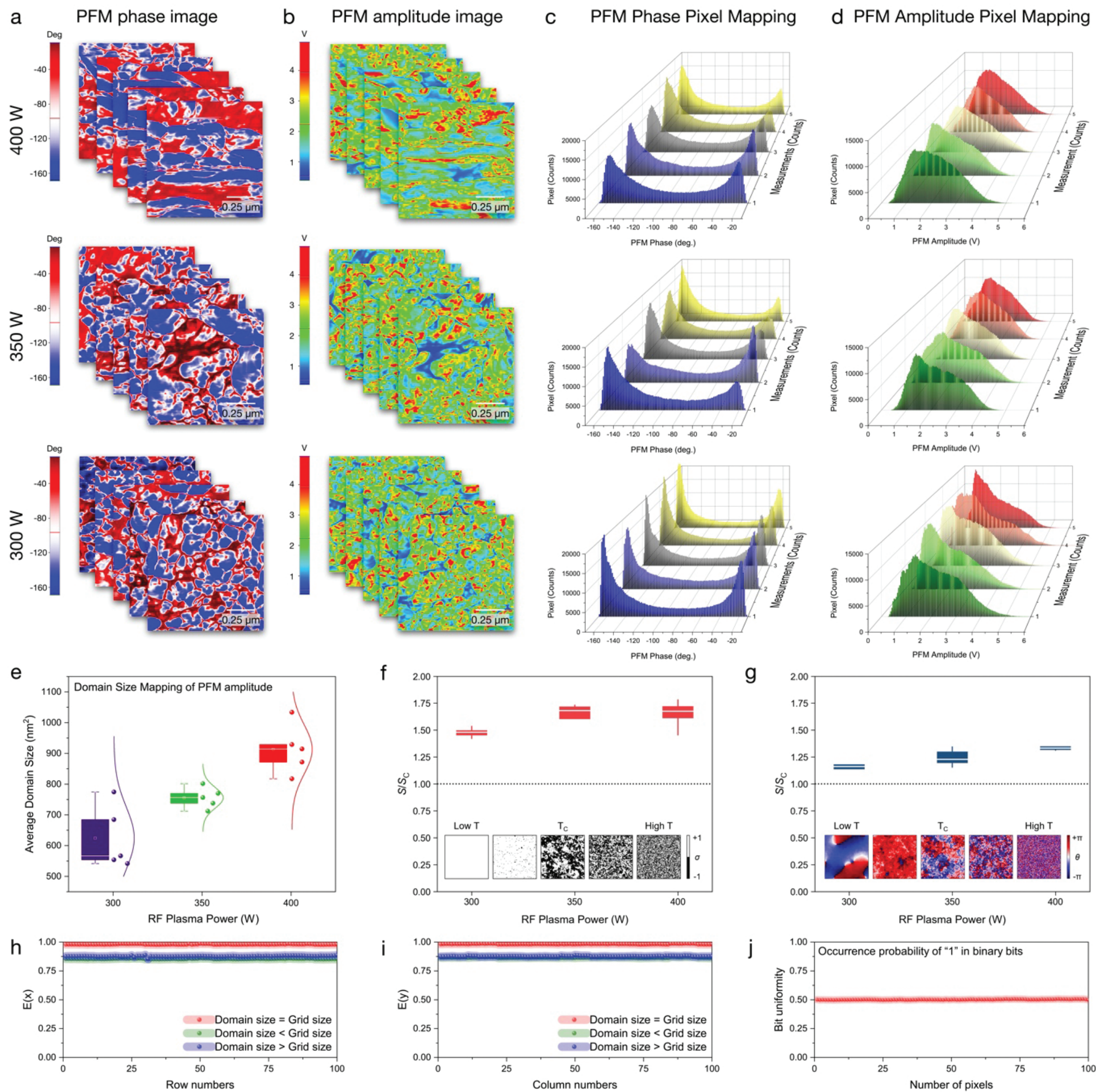

Figure 4. Scalable OOP domain distribution via RF plasma power variation. Spatial OOP domain mapping with a) PFM Phase and b) PFM amplitude with RF plasma power variation. Its corresponding pixel mapping of c) PFM Phase and d) PFM amplitude indicates clear separation in OOP polarization distribution. Statistical evaluation of domain size distribution with e) PFM amplitude, f) Lempel–Ziv entropy of PFM amplitudes, and g) sample entropy of PFM phases. Each entropy measures were normalized by those at the critical point (S_C) of the Ising and XY model, respectively (inset: spin configurations with respect to the temperature). Entropy values along the h) row axe (E(x)) and i) column axe (E(y)) with a comparison of domain size and pixel grid size, resulting in the highest encryption performance at homogenous pixel grid size and domain size. j) Occurrence probability plot of bit "1", which results in 50.12% for bit "1" and 49.88% for bit "0′.

pixel distribution (Figure 4c), and PFM amplitude pixel distribution (Figure 4d). Regarding the sequential domain reconstruction, the separation of OOP polarization is sequentially clarified with OOP domain expansion. While the pristine Bi_2Se_3 exhibited a homogeneous OOP domain distribution, nanoscale OOP domain separation was observed with RF plasma power of 300, 350, and 400 W. The average domain size of negative polarization is distributed as 4560.60 nm^2 (300 W), 6993.30 nm^2 (350 W), and 8084.62 nm^2 (400 W), while positive polarization is distributed as 1860.99 nm^2 (300 W), 3145.24 nm^2 (350 W), and 5455.55 nm^2 (400 W) (Figure S9, Supporting Information). As shown in Figure 4f,g, it was demonstrated that both PFM amplitude and phase at all plasma power exhibit complexity measures that exceed those observed at critical points, suggesting that Janus topological insulators possess a high degree of intrinsic randomness. The intrinsic randomness of the proposed Janus topological insulator was quantified by information theory-based complexity measures and compared against the critical point of spin models where system properties undergo abrupt transitions. The analysis employed two reference 2D spin systems: the Ising model

 © 2025 Wiley-VCH GmbH

15214095, 0, Downloaded from https://advanced.onlinelibrary.wiley.com/doi/10.1002/adma.202419927 by Seoul National University, Wiley Online Library on [25/02/2025]. See the Terms and Conditions (https://onlinelibrary.wiley.com/terms-and-conditions) on Wiley Online Library for rules of use; OA articles are governed by the applicable Creative Commons License

15214095, 0, Downloaded from https://advanced.onlinelibrary.wiley.com/doi/10.1002/adma.202419927 by Seoul National University, Wiley Online Library on [25/02/2025]. See the Terms and Conditions (https://onlinelibrary.wiley.com/terms-and-conditions) on Wiley Online Library for rules of use; OA articles are governed by the applicable Creative Commons License

with discrete binary states (up/down) and the XY model with continuous states, which served as references for PFM amplitude and phase, respectively. To assess the complexity of the reference systems, the Lempel-Ziv entropy (S_{LZ})[41] and sample entropy (S_{samp})[42] were utilized. The average domain size of PFM amplitude results as 624.20 nm^2 (300 W), 755.43 nm^2 (350 W), and 912.95 nm^2 (400 W) (Figure 4e). Increased RF plasma power induces the larger OOP domain distribution and its corresponding domain size distribution. As the average OOP domain size can be calculated as 20 nm (300 W), 40 nm (350 W), and 60 nm (400 W), pixel grid size was controlled with 20 nm × 20 nm, 40 nm × 40 nm, and 60 nm × 60 nm. To further clarify the controllable OOP domain size, entropy value, and its corresponding encryption performance have been evaluated within pixel size variation. As shown in Figure 4h,i, Entropy values along the row axe (E(x)) and column axe (E(y)) have been indicated. Regarding the comparison of domain size and pixel grid size, E(y) value is distributed as 0.982714 (domain size = pixel size), 0.865 (domain size < pixel size), and 0.876 (domain size > pixel size), while E(x) value is distributed as 0.980017 (domain size = pixel size), 0.853 (domain size < pixel size), and 0.878057 (domain size > pixel size). While these values are close to the ideal entropy value of '1', signifying that the Janus PUF results the high levels of unpredictability and encryption performance at homogenous pixel grid size and domain size. Regarding the PUFs operation mechanism, each pixel indicates a balanced chance of resulting in either a zero or one state. Same situation as coin flipping, if a coin with only one side is flipped, the probability of the head (H) or tail (T) side is either '0' or '1', and hence the entropy is '0'. However, in this situation, the probability of obtaining either the "H" or "T" is '0.5', resulting in an entropy value of '1', which generates a perfect random outcome. Hence, a balanced distribution is the most significant factor in the production of a random binary code combination array. While each bit in the binary array has a homogeneous probability (0.5) of being either 0 or 1, an ideal bit uniformity should be converged to 0.5. Figure 4j exhibits the probability distribution of bit "1" from 200 images, resulting in the bit uniformity value of 0.5012 (Figure S10, Supporting Information).

2.5. Challenge-Response Operation of Janus PUFs via Controllable CRPs Size Distribution

The challenge-response authentication process was implemented to evaluate the performance of the Janus PUFs, as illustrated in **Figure** 5a–c. In the challenge-response authentication process, PFM spectroscopy has been utilized to generate and spatially map the CRPs of Janus PUFs. Regarding the challenges in Janus PUFs, responses were generated with independent 2 authentication keys (PFM amplitude (key 1), PFM phase (key 2)). These unique IDs, which are generated through the binarization process of extraction, enable the Janus PUFs to operate as distinctive random-code generators, as shown in Figure 5b. An array of responses (R_1–R_{50}) were spatially mapped via PFM spectroscopy measurements. A digitalization process was performed using a Gabor filter, which classified the response using pre-established threshold values to generate response bits and their corresponding cryptographic keys. To validate the encryption performance of the Janus PUFs, a similarity comparison of different PUFs and the same PUFs was performed as shown in Figure 5d–i. A similarity comparison of PUFs has been performed with a variation of OOP domain size and pixel grid size, which confirms the non-repeatability of different PUFs (Figure S11, Supporting Information) and repeatability of the same PUFs. Based on the similarity between the same PUFs, the performance of Janus PUFs reveals a repeatable response when different PUFs exhibit unique and unclear responses. As the OOP domain size distribution can be controlled with RF plasma power variation, variations of pixel grid size and OOP domain size were concurrently conducted for relative evaluation of encryption performance. Owing to the entropy value comparison of pixel size and domain size, encryption performance similarly exhibits the highest repeatability (same PUFs) and highest non-repeatability (different PUFs, Figure S11, Supporting Information) in homogeneous pixel grid size with domain size (pixel size 20 nm, RF plasma 300 W / pixel size 40 nm, RF plasma 350 W / pixel size 60 nm, RF plasma 400 W). Hence, controllable OOP domain size correlates with encryption performance with pixel grid size variation. Furthermore, randomly selected 400 datasets from the PFM hysteresis curve have been plotted to clarify the reproducibility of PUFs operation and the wake-up effects (Figures S12–S19, Supporting Information).

3. Conclusion

In conclusion, we presented a vdW Janus topological insulator via plasma sulfurization that enables stochastic inversion asymmetry. Owing to the ion bombardment, the Se atom is randomly terminated by the S atom, resulting in sulfur dominance and its corresponding local lattice distortion. By constructing an OOP PFM junction with vdW Janus topological insulator, spatial hysteresis mapping of hysteresis, work function, and adhesion energy experimentally demonstrates sulfur dominance with RF plasma power variation. While the practical application of topological insulators is completely hindered by topological protection, single-step penetrative H_2S^+ ion bombardment activates OOP domain stochasticity, which permits the practical device application of topological insulators that was not previously possible. To take advantage of the stochastic inversion asymmetry, the PUFs application has been presented with size-controllable CRPs generation. In conclusion, we envision that the our Janus PUFs platform can offer an extendable encryption platform with stochastic inversion asymmetry and a single-step synthesis method for vdW topological insulators.

4. Experimental Section

Plasma sulfurization: The ICP-type of plasma-enhanced chemical vapor deposition (ICP-PECVD) (AFS-IC6T, Korea) was used for the sulfurization of Bi_2Se_3 to break its structural symmetry. A high vacuum of ≈5 × 10^{-5} in the PECVD chamber was used to evacuate impurities to achieve clean synthesis without other unexpected reactions before plasma treatment for sulfurization. In this study, only the RF plasma power was controlled from 300 to 400 W under constant gas conditions, and the argon and H_2S flows were maintained at 50 SCCM at a pressure of 25 mTorr at room temperature.

Mechanical Exfoliation and Transfer of 2D Bi_2Se_3: Before mechanical exfoliation and dry transfer, a polydimethylsiloxane stamp was attached to a glass cover. 2D Bi_2Se_3 was mechanically exfoliated from bulk crystals

 © 2025 Wiley-VCH GmbH

15214095, 0, Downloaded from https://advanced.onlinelibrary.wiley.com/doi/10.1002/adma.202419927 by Seoul National University, Wiley Online Library on [25/02/2025]. See the Terms and Conditions (https://onlinelibrary.wiley.com/terms-and-conditions) on Wiley Online Library for rules of use; OA articles are governed by the applicable Creative Commons License

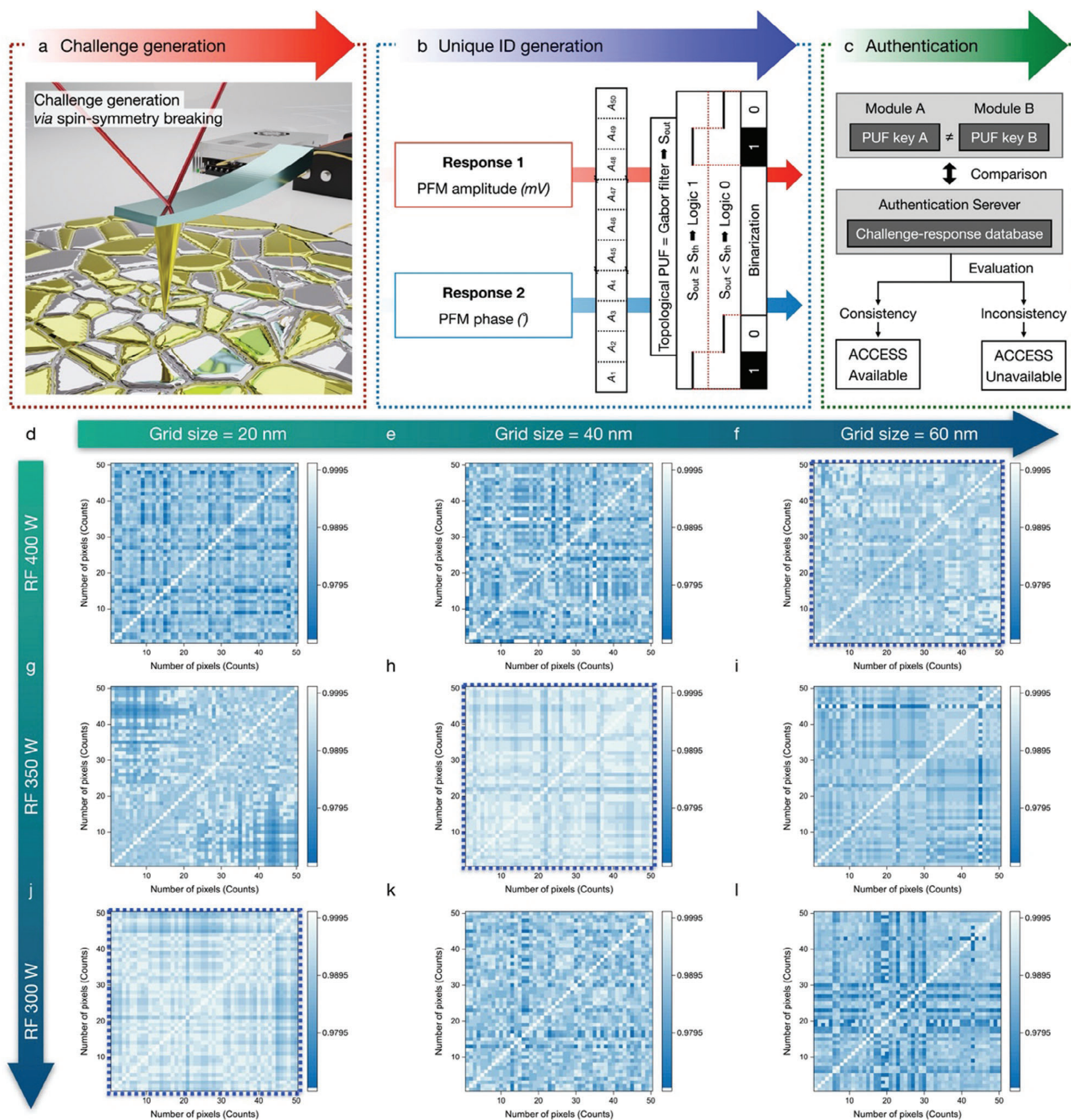

Figure 5. Encryption performance evaluation of Janus PUFs with OOP domain size variation. Schematic illustration of Janus PUFs encryption and authentication process, which consists of a) challenge generation process, b) unique ID generation process, and c) authentication process. To experimentally validate the scalable domain size and its corresponding PUFs performance, a similarity comparison of the same PUFs has been conducted with domain size variation and its corresponding pixel size., which is consisted of d) pixel size 20 nm, RF plasma 400 W, e) pixel size 40 nm, RF plasma 400 W, f) pixel size 60 nm, RF plasma 400 W, g) pixel size 20 nm, RF plasma 350 W, h) pixel size 40 nm, RF plasma 350 W, i) pixel size 60 nm, RF plasma 350 W, j) pixel size 20 nm, RF plasma 400 W, k) pixel size 40 nm, RF plasma 400 W, and l) pixel size 60 nm, RF plasma 400 W. Highest PUFs performance has been clearly observed with homogeneous pixel size with OOP domain size.

(HQ Graphene, Netherlands) onto polydimethylsiloxane stamps and then transferred onto the substrate by applying a transfer condition of 70 °C.

Atomic Force Microscopy: AFM (NX-10 AFM, Park Systems, Republic of Korea) was conducted with an ElectriMulti75E cantilever. A silver paste electrode was selectively deposited on the sample edge to induce vertical charge transfer. The ElectriMulti75-G cantilever was calibrated with a tip radius of 25 nm, a length of 225 µm, a height of 17 µm, a width of 28 µm, and a spring constant of 3.3 N/m, resulting in a resonance frequency of 60.8 kHz. PFM hysteresis and imaging were performed using an AC +5V signal based on the calibrated contact resonance frequency.

Material Characterization: XPS measurements (XIS Supra+, Kratos, United Kingdom) were used to characterize Bi_2Se_3, with an X-ray spot size

15214095, 0, Downloaded from https://advanced.onlinelibrary.wiley.com/doi/10.1002/adma.202419927 by Seoul National University, Wiley Online Library on [25/02/2025]. See the Terms and Conditions (https://onlinelibrary.wiley.com/terms-and-conditions) on Wiley Online Library for rules of use; OA articles are governed by the applicable Creative Commons License

of 400 µm. Peak deconvolution was performed on the Bi 4*f*, Se 2*p*, and S 2*p* signals, with the profiles aligned using the C 1s peak at 285 eV. The XPS data were calibrated using the CASAXPS software (version 8.1). Optical microscopy (U-MSSP4, Olympus, Japan) and FE-SEM (S-4800, Hitachi, Japan) were used to examine the transferred flakes. For cross-sectional TEM specimen preparation, a focused ion beam instrument (NX2000, Hitachi Ltd., Japan) was used, employing a Ga^+ ion beam (30–5 keV) and a lift-off process to etch the specimens. TEM (JEM-2100F, JEOL, Japan) and XRD (Empyrean, Malvern PANalytical, United Kingdom) were used to observe the lattice structure, EDS, and SAED patterns of the layered Bi_2Se_3 structures at the atomic scale.

Entropy calculation: Lempel-Ziv entropy (S_{LZ}) is the normalized complexity of a given string with length N. For the n-digit sequence of length N, S_{LZ} can be calculated as follows:

$$S_{LZ} = \frac{C_{LZ}\log_n N}{N} \tag{4}$$

where C_{LZ} is a Lempel-Ziv complexity.

Sample entropy (S_{samp}) quantifies the randomness of the signal based on the distance. First, the sequence $\mathbf{X}$ of length N is segmented into subsequences $\mathbf{X}_{m,i}$ with the embedding dimension m.

Here, two sequences can be considered to be equal if the Chebyshev distance (d_∞) between two sequences is under the threshold r. The subsequence similarity was evaluated using the correlation integral $C_{m,i}(r)$, which calculates the probability of finding subsequences comparable to subsequence i.

$$d_\infty\left(X_m, Y_m\right) = \lim_{p\to\infty}\left[\sum_{k=1}^{m}\left(X_k - Y_k\right)^p\right]^{\frac{1}{p}} = \max_{k\in[1,m]}\left|X_k - Y_k\right| \tag{5}$$

$$C_{m,i}(r) = \frac{1}{N-m+1}\sum_{j=1}^{N-m+1} u\left(r - d_\infty\left(X_{m,i}, X_{m,j}\right)\right) \tag{6}$$

where $u(\cdot)$ indicates the Heaviside function.

S_{samp} is calculated from correlation integral by evaluating the frequency of similar subsequences across embedding dimensions m and m+1. Therefore, S_{samp} can measure the signal complexity, since high prevalence of unique patterns corresponds to increased complexity in the system.

$$S_{samp} = \log \frac{\sum_{i=1}^{N-m}\sum_{j=1,j\neq i}^{N-m} u\left(r - d_\infty\left(X_{m,i}, X_{m,j}\right)\right)}{\sum_{i=1}^{N-m}\sum_{j=1,j\neq i}^{N-m} u\left(r - d_\infty\left(X_{m+1,i}, X_{m+1,j}\right)\right)} \tag{7}$$

Supporting Information

Supporting Information is available from the Wiley Online Library or from the author.

Acknowledgements

This research was supported by the Basic Science Research Program of the National Research Foundation of Korea (NRF) funded by the Ministry of Education (No. 2022R1A3B1078163). This study was supported by the Institute for Basic Science (grant number IBS-R027-D1). This research was funded and conducted under the Competency Development Program for Industry Specialists of the Korean Ministry of Trade, Industry, and Energy (MOTIE), operated by the Korea Institute for Advancement of Technology (KIAT) (No. P0023704, Semiconductor-Track Graduate School (SKKU)). This work was supported by the Korean Collaborative & High-tech Initiative for Prospective Semiconductor Research (K-CHIPS) (KEIT1415187508, 20024772), funded by the Ministry of Trade, Industry & Energy (MOTIE, Korea). This study was supported by the MOTIE (Ministry of Trade, Industry, and Energy (grant number 1415187508) for the development of future semiconductor devices. This study was supported by the National Research Foundation (NRF) funded by the Korean government (MSIT) (No. RS-2024-00437142). This work was supported by the Technology Innovation Program (20017367, Development of precise manufacturing technology for CMP pad conditioners), funded By the Ministry of Trade, Industry & Energy (MOTIE, Korea). This work was supported by the Technology Innovation Program (00144020, Abatement of the industrial processing gases or combination odors using multi-staged nano-sec pulse corona discharge reaction) funded By the Ministry of Trade, Industry & Energy (MOTIE, Korea). This work was supported by National Research Foundation of Korea (No. RS-2024-00433633)

Conflict of Interest

The authors declare no conflict of interest.

Author Contributions

G.K., J.L., H.S., and T.K. contributed equally to this study. G.K., J.L., and H.S. prepared samples and performed experiments. T.K. conducted entropy calculation and PUFs performance evaluation. D.L. and S.S. performed the Raman spectroscopy measurements. J.C., G.W., and S.S. were involved in technical discussions on the PUFs. H.S., S.H., H.C., H.H., J.C., S.L., and S.S.conducted the analytical experiments, including TEM, EDS, in situ XRD, and in situ XPS measurements. G.H., G.J., and Y.L. provided technical advice on the AFM system. M.L., J.P., A. O, Y. K., L. F., A. H., W. J. analyzed and discussed the experimental results with J.L., G.K., J.L., H.S., and T.K. wrote the manuscript with contributions from all the authors. S.K. and T.K. designed and supervised the study. All the authors have read and approved the final version of this manuscript.

Data Availability Statement

The data that support the findings of this study are available from the corresponding author upon reasonable request.

Keywords

out-of-plane polarization, physically unclonable functions, piezoelectric force microscopy, plasma sulfurization, topological insulator

Received: December 18, 2024
Revised: January 21, 2025
Published online:

[1] a) M. A. Bandres, S. Wittek, G. Harari, M. Parto, J. Ren, M. Segev, D. N. Christodoulides, M. Khajavikhan, *Science* **2018**, *359*, eaar4005; b) S. Chen, A. Bylinkin, Z. Wang, M. Schnell, G. Chandan, P. Li, A. Y. Nikitin, S. Law, R. Hillenbrand, *Nat. Commun.* **2022**, *13*, 1374; c) C. He, H. S. Lai, B. He, S. Y. Yu, X. Xu, M. H. Lu, Y. F. Chen, *Nat. Commun.* **2020**, *11*, 2318; d) D. Hsieh, Y. Xia, D. Qian, L. Wray, J. Dil, F. Meier, J. Osterwalder, L. Patthey, J. Checkelsky, N. P. Ong, *Nature* **2009**, *460*, 1101.

[2] a) E. A. A. Pogna, L. Viti, A. Politano, M. Brambilla, G. Scamarcio, M. S. Vitiello, *Nat. Commun.* **2021**, *12*, 6672; b) B. Singh, H. Lin, A. Bansil, *Adv. Mater.* **2023**, *35*, 2201058.

[3] P. Corbae, S. Ciocys, D. Varjas, E. Kennedy, S. Zeltmann, M. Molina-Ruiz, S. M. Griffin, C. Jozwiak, Z. Chen, L. W. Wang, *Nat. Mater.* **2023**, *22*, 200.

© 2025 Wiley-VCH GmbH

[4] Y. Sha, J. Zheng, K. Liu, H. Du, K. Watanabe, T. Taniguchi, J. Jia, Z. Shi, R. Zhong, G. Chen, *Science* **2024**, *384*, 414.
[5] a) A. Fritzsche, T. Biesenthal, L. J. Maczewsky, K. Becker, M. Ehrhardt, M. Heinrich, R. Thomale, Y. N. Joglekar, A. Szameit, *Nat. Mater.* **2024**, *23*, 377; b) Z. Ren, D. Liu, E. Zhao, C. He, K. K. Pak, J. Li, G. B. Jo, *Nat. Phys.* **2022**, *18*, 385; c) M. Kim, Z. Wang, Y. Yang, H. T. Teo, J. Rho, B. Zhang, *Nat. Commun.* **2022**, *13*, 3499.
[6] a) R. Jain, M. Stanley, A. Bose, A. R. Richardella, X. S. Zhang, T. Pillsbury, D. A. Muller, N. Samarth, D. C. Ralph, *Sci. Adv.* **2023**, *9*, eadi4540; b) Q. L. He, T. L. Hughes, N. P. Armitage, Y. Tokura, K. L. Wang, *Nat. Mater.* **2022**, *21*, 15; c) P. He, H. Isobe, D. Zhu, C. H. Hsu, L. Fu, H. Yang, *Nat. Commun.* **2021**, *12*, 698; d) M. M. Otrokov, I. I. Klimovskikh, H. Bentmann, D. Estyunin, A. Zeugner, Z. S. Aliev, S. Gaß, A. Wolter, A. Koroleva, A. M. Shikin, *Nature* **2019**, *576*, 416.
[7] a) C. W. Peterson, T. Li, W. Jiang, T. L. Hughes, G. Bahl, *Nature* **2021**, *589*, 376; b) I. Di Bernardo, J. Hellerstedt, C. Liu, G. Akhgar, W. Wu, S. A. Yang, D. Culcer, S. K. Mo, S. Adam, M. T. Edmonds, *Adv. Mater.* **2021**, *33*, 2005897.
[8] J. Liu, F. Xia, D. Xiao, F. J. Garcia de Abajo, D. Sun, *Nat. Mater.* **2020**, *19*, 830.
[9] a) M. Chen, Y. Xie, B. Cheng, Z. Yang, X. Z. Li, F. Chen, Q. Li, J. Xie, K. Watanabe, T. Taniguchi, *Nat. Nanotechnol.* **2024**, *19*, 962; b) C. Yin, C. Gong, S. Tian, Y. Cui, X. Wang, Y. Wang, Z. Hu, J. Huang, C. Wu, B. Chen, *Adv. Funct. Mater.* **2022**, *32*, 2108455.
[10] Z. Liu, P. Jin, M. Lei, C. Wang, F. Marchesoni, J. H. Jiang, J. Huang, *Nat. Rev. Phys.* **2024**, *6*, 554.
[11] J. W. You, Q. Ma, Z. Lan, Q. Xiao, N. C. Panoiu, T. J. Cui, *Nat. Commun.* **2021**, *12*, 5468.
[12] L. Powalla, M. T. Birch, K. Litzius, S. Wintz, F. S. Yasin, L. A. Turnbull, F. Schulz, D. A. Mayoh, G. Balakrishnan, M. Weigand, *Adv. Mater.* **2023**, *35*, 2208930.
[13] S. Chen, S. Yuan, Z. Hou, Y. Tang, J. Zhang, T. Wang, K. Li, W. Zhao, X. Liu, L. Chen, *Adv. Mater.* **2021**, *33*, 2000857.
[14] a) K. X. Zhang, H. Ju, H. Kim, J. Cui, J. Keum, J. G. Park, J. S. Lee, *Adv. Mater.* **2024**, *36*, 2312824; b) Q. Fu, X. Cong, X. Xu, S. Zhu, X. Zhao, S. Liu, B. Yao, M. Xu, Y. Deng, C. Zhu, *Adv. Mater.* **2023**, *35*, 2306330.
[15] Z. Hu, L. Zhang, A. Chakraborty, G. D'Olimpio, J. Fujii, A. Ge, Y. Zhou, C. Liu, A. Agarwal, I. Vobornik, *Adv. Mater.* **2023**, *35*, 2209557.
[16] a) L. Molino, L. Aggarwal, V. Enaldiev, R. Plumadore, V. I. Fal´ko, A. Luican-Mayer, *Adv. Mater.* **2023**, *35*, 2207816; b) Q. Li, C. X. Trang, W. Wu, J. Hwang, D. Cortie, N. Medhekar, S. K. Mo, S. A. Yang, M. T. Edmonds, *Adv. Mater.* **2022**, *34*, 2107520.
[17] J. Lee, G. Woo, J. Cho, S. Son, H. Shin, H. Seok, M. J. Kim, E. Kim, Z. Wang, B. Kang, *Nat. Commun.* **2024**, *15*, 5162.
[18] Z. Liang, X. Zhou, L. Zhang, X. L. Yu, Y. Lv, X. Song, Y. Zhou, H. Wang, S. Wang, T. Wang, *Nat. Commun.* **2023**, *14*, 4230.
[19] a) H. Yi, L. H. Hu, Y. Wang, R. Xiao, J. Cai, D. R. Hickey, C. Dong, Y. F. Zhao, L. J. Zhou, R. Zhang, *Nat. Mater.* **2022**, *21*, 1366; b) R. Rechciński, M. Galicka, M. Simma, V. V. Volobuev, O. Caha, J. Sánchez-Barriga, P. S. Mandal, E. Golias, A. Varykhalov, O. Rader, *Adv. Funct. Mater.* **2021**, *31*, 2008885.
[20] a) L. Li, Y. Wu, X. Liu, J. Liu, H. Ruan, Z. Zhi, Y. Zhang, P. Huang, Y. Ji, C. Tang, *Adv. Mater.* **2023**, *35*, 2207322; b) Y. Li, J. Zhang, Q. Chen, X. Xia, M. Chen, *Adv. Mater.* **2021**, *33*, 2100855.
[21] D. Xie, G. Gao, B. Tian, Z. Shu, H. Duan, W. W. Zhao, J. He, J. Jiang, *Adv. Mater.* **2023**, *35*, 2212118.
[22] J. Wen, W. Tang, Z. Kang, Q. Liao, M. Hong, J. Du, X. Zhang, H. Yu, H. Si, Z. Zhang, *Adv. Sci.* **2021**, *8*, 2101417.
[23] R. Zhang, M. Li, L. Li, Z. Wei, F. Jiao, D. Geng, W. Hu, *Adv. Funct. Mater.* **2021**, *31*, 2102049.
[24] a) Y. Ding, C. Wang, M. Zeng, L. Fu, *Adv. Mater.* **2023**, 2306689; b) Y. Qin, M. Sayyad, A. R. P. Montblanch, M. S. Feuer, D. Dey, M. Blei, R. Sailus, D. M. Kara, Y. Shen, S. Yang, *Adv. Mater.* **2022**, *34*, 2106222; c) H. Li, Y. Qin, B. Ko, D. B. Trivedi, D. Hajra, M. Y. Sayyad, L. Liu, S. H. Shim, H. Zhuang, S. Tongay, *Adv. Mater.* **2020**, *32*, 2002401.
[25] a) M. Sayyad, J. Kopaczek, C. M. Gilardoni, W. Chen, Y. Xiong, S. Yang, K. Watanabe, T. Taniguchi, R. Kudrawiec, G. Hautier, *Adv. Mater.* **2024**, *36*, 2403583; b) D. B. Trivedi, G. Turgut, Y. Qin, M. Y. Sayyad, D. Hajra, M. Howell, L. Liu, S. Yang, N. H. Patoary, H. Li, *Adv. Mater.* **2020**, *32*, 2006320.
[26] Y. C. Lin, C. Liu, Y. Yu, E. Zarkadoula, M. Yoon, A. A. Puretzky, L. Liang, X. Kong, Y. Gu, A. Strasser, *ACS Nano* **2020**, *14*, 3896.
[27] X. Wan, E. Chen, J. Yao, M. Gao, X. Miao, S. Wang, Y. Gu, S. Xiao, R. Zhan, K. Chen, *ACS Nano* **2021**, *15*, 20319.
[28] Z. Gan, I. Paradisanos, A. Estrada-Real, J. Picker, E. Najafidehaghani, F. Davies, C. Neumann, C. Robert, P. Wiecha, K. Watanabe, *Adv. Mater.* **2022**, *34*, 2205226.
[29] a) H. Seok, Y. T. Megra, C. K. Kanade, J. Cho, V. K. Kanade, M. Kim, I. Lee, P. J. Yoo, H. U. Kim, J. W. Suk, *ACS Nano* **2021**, *15*, 707; b) L. Zhang, Z. Yang, T. Gong, R. Pan, H. Wang, Z. Guo, H. Zhang, X. Fu, *J. Mater. Chem. A* **2020**, *8*, 8813.
[30] S. Li, D. Ouyang, N. Zhang, Y. Zhang, A. Murthy, Y. Li, S. Liu, T. Zhai, *Adv. Mater.* **2023**, *35*, 2211855.
[31] C. Wu, X. L. Shi, M. Li, Z. Zheng, L. Zhu, K. Huang, W. D. Liu, P. Yuan, L. Cheng, Z. G. Chen, *Adv. Funct. Mater.* **2024**, *34*, 2402317.
[32] S. Li, F. Wang, Y. Wang, J. Yang, X. Wang, X. Zhan, J. He, Z. Wang, *Adv. Mater.* **2024**, *36*, 2301472.
[33] W. Yang, G. Tian, H. Fan, Y. Zhao, H. Chen, L. Zhang, Y. Wang, Z. Fan, Z. Hou, D. Chen, *Adv. Mater.* **2022**, *34*, 2107711.
[34] A. B. Puthirath, X. Zhang, A. Krishnamoorthy, R. Xu, F. S. Samghabadi, D. C. Moore, J. Lai, T. Zhang, D. E. Sanchez, F. Zhang, *Adv. Mater.* **2022**, *34*, 2206425.
[35] a) Z. Zhang, S. Liu, Q. Pan, Y. Hong, Y. Shan, Z. Peng, X. Xu, B. Liu, Y. Chai, Z. Yang, *Adv. Mater.* **2022**, *34*, 2200864; b) C. Di Giorgio, E. Blundo, G. Pettinari, M. Felici, F. Bobba, A. Polimeni, *Adv. Mater. Interfaces* **2022**, *9*, 2102220.
[36] W. B. Jung, S. Jang, S. Y. Cho, H. J. Jeon, H. T. Jung, *Adv. Mater.* **2020**, *32*, 1907101.
[37] a) Y. Miao, X. Zhou, Z. Wang, X. Liu, Y. Yuan, Y. Jing, H. Luo, D. Zhang, J. Sun, *Adv. Funct. Mater.* **2024**, *34*, 2314883; b) Q. Li, F. Chen, J. Su, Y. Yao, J. Kang, F. Xie, M. Li, J. Zhang, *Adv. Funct. Mater.* **2024**, 2416216; c) H. Guo, Y. Qin, Z. Wang, Y. Ma, H. Wen, Z. Li, Z. Ma, X. Li, J. Tang, J. Liu, *Adv. Funct. Mater.* **2024**, *34*, 2304648.
[38] a) S. Falcinelli, F. Pirani, F. Vecchiocattivi, *Atmosphere* **2015**, *6*, 299; b) H. Seok, M. Kim, J. Cho, E. Kim, S. Son, K. W. Kim, J. K. Kim, P. J. Yoo, M. Kim, H. U. Kim, *ACS Sustainable Chem. Eng.* **2023**, *11*, 568.
[39] H. Seok, I. Lee, J. Cho, D. Sung, I. K. Baek, C. H. Lee, E. Kim, S. Jeon, K. Park, T. Kim, *Nanotechnology* **2021**, *33*, 025603.
[40] J. Lee, G. Woo, G. Lee, J. Jeon, S. Lee, Z. Wang, H. Shin, G. W. Lee, Y. J. Kim, D. H. Lee, *ACS Appl. Mater. Interfaces* **2024**, *16*, 35505.
[41] A. Lempel, J. Ziv, *IEEE Trans. Inf. Theory* **1976**, *22*, 75.
[42] a) S. M. Pincus, *Proc. Natl. Acad. Sci. USA* **1991**, *88*, 2297; b) J. S. Richman, J. R. Moorman, *Am. J. Physiol.: Heart Circ. Physiol.* **2000**, *278*, H2039.

 © 2025 Wiley-VCH GmbH

15214095, 0, Downloaded from https://advanced.onlinelibrary.wiley.com/doi/10.1002/adma.202419927 by Seoul National University, Wiley Online Library on [25/02/2025]. See the Terms and Conditions (https://onlinelibrary.wiley.com/terms-and-conditions) on Wiley Online Library for rules of use; OA articles are governed by the applicable Creative Commons License